



Title	Model equations of light scattering properties and a characteristic time of light propagation for polydisperse colloidal suspensions at different volume fractions
Author(s)	Fujii, Hiroyuki; Ueno, Moegi; Inoue, Yuki; Aoki, Toshiaki; Kobayashi, Kazumichi; Watanabe, Masao
Citation	Optics Express, 30(3), 3538-3552 <a href="https://doi.org/10.1364/OE.447334">https://doi.org/10.1364/OE.447334</a>
Issue Date	2022-01-31
Doc URL	<a href="http://hdl.handle.net/2115/83934">http://hdl.handle.net/2115/83934</a>
Rights	© 2022 Optical Society of America. Users may use, reuse, and build upon the article, or use the article for text or data mining, so long as such uses are for non-commercial purposes and appropriate attribution is maintained. All other rights are reserved.
Type	article
File Information	oe-30-3-3538.pdf



[Instructions for use](#)



# Model equations of light scattering properties and a characteristic time of light propagation for polydisperse colloidal suspensions at different volume fractions

HIROYUKI FUJII,\*  MOEGI UENO, YUKI INOUE, TOSHIAKI AOKI, KAZUMICHI KOBAYASHI, AND MASAO WATANABE

*Division of Mechanical and Space Engineering, Faculty of Engineering, Hokkaido University, Kita 13 Nishi 8, Kita-ku, Sapporo, Hokkaido 060-8628, Japan*

\*[fujii-hr@eng.hokudai.ac.jp](mailto:fujii-hr@eng.hokudai.ac.jp)

**Abstract:** We developed model equations of light scattering properties and a characteristic time of light propagation for polydisperse colloidal suspensions at different volume fractions. By the model equations, we examined numerical results using the first-order (dependent) scattering theory (FST) and radiative transfer theory in 600-980 nm wavelength. The model equations efficiently treat the interference of electric fields scattered from colloidal particles by a single effective coefficient, providing fast computation. Meanwhile, the FST provides accurate but complicated treatment. We found the interference effects on the scattering properties and characteristic time depend linearly on wavelength. Dimensionless analysis showed a simple mechanism of the interference effects, independently of wavelength and source-detector distance.

© 2022 Optica Publishing Group under the terms of the [Optica Open Access Publishing Agreement](#)

## 1. Introduction

Dense media such as biological tissues and colloidal suspensions scatter light strongly, and the light propagation direction changes many times in the media [1–3]. Quantitative understanding of light scattering and light propagation in dense media is indispensable for various research fields such as biomedical optics [1], remote sensing [4], and photocatalysis [5]. The understanding leads to further improvement for imaging techniques using scattered light, e.g., near-infrared imaging and spectroscopy for a deep region in the media [6–9]. For the understanding, accurate determinations of the scattering properties are crucial. Usually, the scattering properties are determined by the inverse analysis based on the radiative transfer theory (RTT) [10–12]. The inverse analysis minimizes a difference in light intensity between measurement data and computational results by the RTT. The RTT describes light propagation in terms of light scattering and absorption on a macroscopic scale [7,13,14], where a medium size is much larger than the optical wavelength. On the macroscopic scale, a medium can be considered a continuous medium. Meanwhile, the scattering properties are calculated from the electromagnetic theory (EMT) on a microscopic scale, where a system size is comparable to the wavelength. On the microscopic scale, a medium is regarded as a system consisting of discrete particles in a background medium.

The scattering properties for colloidal suspensions have been extensively examined by the EMT [15–17] as basic research for biological tissues and agricultural products. As the EMT, the zeroth-order scattering and first-order scattering theories (ZST and FST) have been widely employed and they are based on the zeroth-order and first-order solutions of the Foldy-Lax equation (FLE). The FLE is the multiple scattering expansion of the Maxwell equations [18,19]. The two theories are conventionally called independent and dependent scattering theories, respectively. In this paper, however, we call the two theories as the ZST and FST to avoid the ambiguous terms of "independent" and "dependent" based on the Ref. [20], which pointed out the ambiguity. The ZST considers no interaction of electric fields scattered by colloidal particles

[4,21]. Meanwhile, the FST considers the interaction and treats the interference induced by a superposition of the fields by the colloidal particles in the far-field [4,21]. At a low volume fraction of the colloidal particles, approximately less than 5%, the scattering properties calculated from the ZST nicely agree with experimental results by the inverse analysis [22]. At a high volume fraction up to approximately 20%, meanwhile, the numerical results using the FST agree with experimental results [23]. This fact means that the interference, considered for the FST, is dominant in multiple scattering processes of the fields. It is noted that the concept of "multiple scattering of electric fields" is quite different from that of "multiple scattering of light". The former is rigorously described by the FLE on the microscopic scale, while the latter is usually described by the RTT on the macroscopic scale [1,21].

The interference effect on the scattering properties has been extensively discussed since the 1980s by the FST [17,23–31]. Recently, we have developed a light propagation model based on the RTT combined with FST (RTT-FST) [29], also called a dense media radiative transfer model [21]. The developed light propagation model uses the analytical solution of the RTT for an infinite medium. We have shown the interference effects on light propagation for monodisperse and polydisperse systems (silica suspension and Intralipid-10%) but at a single optical wavelength. Despite many efforts, the interference effects have not been fully understood because of their complicated dependence on the optical wavelength, particle size distribution, and intermolecular interaction. In addition, contributions of the interference to the scattering properties are coupled with those of the single-particle scattering. These facts make it difficult to elucidate the interference effects. For the elucidation, the development of model equations for the scattering properties and light propagation is desirable. The model equations enable evaluating factors of the interference and single-particle scattering, separately.

This study develops newly the model equations for the scattering properties and a peak time of the fluence rate (one of the characteristic times of light propagation) in polydisperse systems. Once we developed the model equations for polydisperse systems, it is straightforward to develop them for monodisperse systems. By the model equations, we investigate the numerical results using the FST and RTT-FST in polydisperse colloidal suspensions (Intralipid-20%) at different volume fractions from 0.1 to 20% in the near-infrared wavelength range from 600 to 980 nm. We employed the light propagation model based on the RTT-FST for the semi-infinite medium, extended from the model for the infinite medium developed in our previous study [29]. Intralipid has been widely used to study the scattering properties as basic research for biological tissues, which are generally polydisperse systems [15,16,22,27]. We examine the factors of the interference and their dependence on the wavelength.

## 2. Theories for the scattering properties and light propagation

As shown in Fig. 1, we consider the scattering properties for a polydisperse colloidal suspension on the microscopic scale and light propagation for the medium on the macroscopic scale. On the microscopic scale (micrometer-scale, Fig. 1(a)), the system consists of discrete colloidal particles and continuous background (water), and the electromagnetic theory (EMT) describes the scattering properties. On the macroscopic scale (centimeter-scale, Fig. 1(b)), the system is regarded as a homogeneous random medium (continuous medium) with constant values of optical properties (scattering properties and absorption coefficient), and the radiative transfer theory (RTT) describes light propagation.

### 2.1. Electromagnetic theory (EMT) for a polydisperse colloidal suspension

We have developed the first-order and zeroth-order scattering theories (FST and ZST) for a polydisperse colloidal suspension based on the Foldy-Lax equation (FLE) [29]. The FST and ZST are obtained from the particle configuration average to the first-order and zeroth-order solutions of the FLE, respectively. From the FST and ZST, we calculated the scattering properties: the

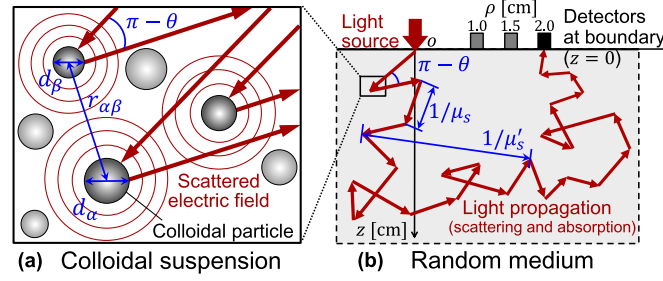


**Fig. 1.** Schematic of electromagnetic scattering for a microscopic-scale colloidal suspension and light propagation for a macroscopic-scale suspension: (a) electric fields scattered by discrete colloidal particles in a continuous background (water), (b) radiative transfer in a homogeneous random medium (continuous medium) by irradiating light source on the surface. The directions with the scattering angle  $\pi - \theta$  are displayed in the figure (a), although the electric fields are scattered in various directions.

phase function  $P(\theta, \phi)$ , scattering coefficient  $\mu_s$ , anisotropy factor  $g$ , and reduced scattering coefficient  $\mu'_s$ . We consider a size-polydisperse system with  $N_s$ -kinds of particle diameters. The total number of the particles  $N$  for the system is given as  $\sum_{\alpha=1}^{N_s} N_\alpha$ , and  $N_\alpha$  is the total number of particles for the  $\alpha$ -class of diameter  $d_\alpha$  ( $\alpha = 1, 2, \dots, N_s$ ). In the FST and ZST, we used the spherical coordinates  $(\theta, \phi)$  with the polar angle  $\theta \in [0, \pi]$  and azimuthal angle  $\phi \in [0, 2\pi]$ . We set the scattering angle to be the same as the polar angle  $\theta$  as shown in Fig. 1(a). We review the FST and ZST here. For the details of the theories, see the reference (our previous work) [29], where the FST and ZST are called the dependent and independent scattering theories, respectively. In this study, we investigate the numerical results for the FST by model equations developed here.

### 2.1.1. First-order scattering theory (FST)

The phase function  $P_F(\theta, \phi)$  for the FST is given as [29]

$$P_F(\theta, \phi) = \sum_{\alpha=1}^{N_s} n_\alpha |\mathbf{F}_\alpha^{Mie}(\theta, \phi)|^2 + \sum_{\alpha=1}^{N_s} \sum_{\beta=1}^{N_s} \sqrt{n_\alpha n_\beta} \mathbf{F}_\alpha^{Mie}(\theta, \phi) \cdot \mathbf{F}_\beta^{Mie*}(\theta, \phi) H_{\alpha\beta}(\theta), \quad (1)$$

where  $n_\alpha$  or  $n_\beta$  is the number density for the  $\alpha$ -class or the  $\beta$ -class ( $\beta = 1, 2, \dots, N_s$ );  $\mathbf{F}_\alpha^{Mie}(\theta, \phi)$  is the scattering amplitude vector using the Mie theory [32];  $\mathbf{F}_\beta^{Mie*}(\theta, \phi)$  is the complex conjugate of  $\mathbf{F}_\beta^{Mie}(\theta, \phi)$  for the  $\beta$ -class; and  $H_{\alpha\beta}(\theta)$  is the Fourier transform of the total correlation function  $H_{\alpha\beta}(r_{\alpha\beta})$  for a pair of the classes  $\alpha - \beta$  as a function of the distance  $r_{\alpha\beta}$  between the two particles as shown in Fig. 1(a). The second term of the right-hand side of Eq. (1) corresponds to the interference of the scattered fields but coupled to the contribution from the single-particle scattering represented by  $\mathbf{F}_\alpha^{Mie} \cdot \mathbf{F}_\beta^{Mie*}$ . For calculations of  $H_{\alpha\beta}(\theta)$ , we employed the polydisperse Percus-Yevick (PY) model [33,34]. Previous researches [23,30,31] showed that the scattering properties for the FST with the PY model agree well with the measurement results for hard-sphere-like colloidal suspensions such as silica and polystyrene suspensions. The scattering coefficient  $\mu_{s,F}$  for the FST is given by integrating  $P_F(\theta, \phi)$  over the whole solid angle:

$$\mu_{s,F} = \sum_{\alpha=1}^{N_s} n_\alpha \sigma_\alpha^{Mie} + \int_0^\pi d\theta \int_0^{2\pi} d\phi \sin \theta \sum_{\alpha=1}^{N_s} \sum_{\beta=1}^{N_s} \sqrt{n_\alpha n_\beta} \mathbf{F}_\alpha^{Mie}(\theta, \phi) \cdot \mathbf{F}_\beta^{Mie*}(\theta, \phi) H_{\alpha\beta}(\theta), \quad (2)$$

where  $\sigma_{\alpha}^{Mie}$  is the scattering cross section for the  $\alpha$ -class using the Mie theory [32]. The anisotropy factor  $g_F$  and reduced scattering coefficients  $\mu'_{s,F}$  for the FST are given as

$$g_F = 2\pi[\mu_{s,F}]^{-1} \int_0^{\pi} d\theta \sin \theta \cos \theta P_F(\theta), \quad (3)$$

$$\mu'_{s,F} = 2\pi \int_0^{\pi} d\theta \sin \theta [1 - \cos \theta] P_F(\theta), \quad (4)$$

where  $P_F(\theta) = (2\pi)^{-1} \int_0^{2\pi} d\phi P_F(\theta, \phi)$ .

### 2.1.2. Zeroth-order scattering theory (ZST)

The phase function  $P_Z(\theta, \phi)$  for the ZST is obtained by omitting the second term of the right hand side in Eq. (1):  $\sum_{\alpha} n_{\alpha} |\mathbf{F}_{\alpha}^{Mie}|^2 = \eta \sum_{\alpha} f_{\alpha} |\mathbf{F}_{\alpha}^{Mie}|^2 / v_0$ , with the volume fraction  $\eta$ , the fraction of particles  $f_{\alpha}$  for the  $\alpha$ -class and  $v_0 = \sum_{\alpha} \pi d_{\alpha}^3 f_{\alpha} / 6$ . Because  $f_{\alpha} |\mathbf{F}_{\alpha}^{Mie}|^2 / v_0$  is independent of  $\eta$ ,  $P_Z(\theta, \phi)$  is linearly proportional to  $\eta$ . From  $P_Z(\theta, \phi)$ , we calculated the scattering properties for the ZST represented by  $\mu_{s,Z}$ ,  $g_Z$ , and  $\mu'_{s,Z}$ . For the explicit forms of the scattering properties for the ZST, see the Refs. [22,29], where the ZST is called the independent scattering theory.

### 2.1.3. Numerical conditions for the FST and ZST

We consider Intralipid-20% (Fresenius-Kabi) as a polydisperse colloidal suspension in water. In Intralipid, the soybean oil encapsulated by lecithin is regarded as a spherical particle (scatterer) [22]. We assumed particles of Intralipid to be hard spheres and used the PY model. This assumption is validated in Sec. 3.2 by comparing the numerical results for the FST with the measurement results in Intralipid. Figure 2(a) displays the particle size distribution  $f_{\alpha}$  of Intralipid [35] with the mean diameter  $d_{mean}$  of 214.3 nm and  $N_s = 34$ . Here,  $f_{\alpha}$  is normalized so as to satisfy the condition of  $\sum_{\alpha=1}^{N_s} f_{\alpha} = 1$ . We varied the volume fraction  $\eta$  [%]: 0.1, 1, 2,  $\dots$ , 20 at equal intervals of 1% in the range 1-20%; and changed the wavelength  $\lambda$  [nm] in the near-infrared wavelength range: 600, 640, 680, 720, 759, 785, 820, 860, 900, 940, 980. We calculated the wavelength-dependence of refractive indices  $n_s$  and  $n_w$  of the colloidal particle and water by the Cauchy equation [22]. In the wavelength range, the  $n_s$ -value decreases from 1.474 to 1.462, and the  $n_w$ -value from 1.334 to 1.322. In our study, the size parameter  $x_s = \pi d_{mean} / (\lambda n_w)$  ranges from 0.91 to 1.50.

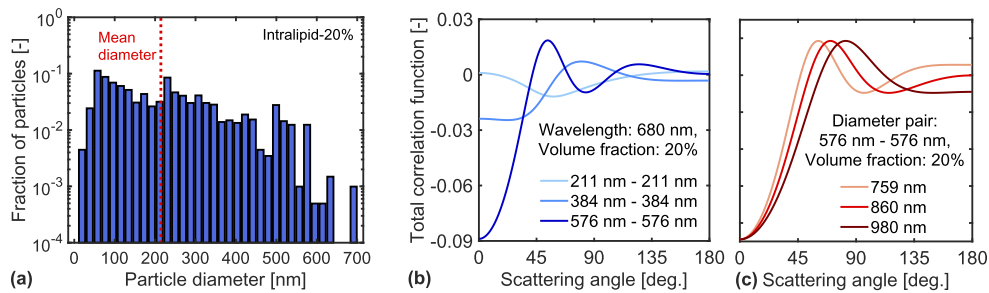


**Fig. 2.** (a) Particle size distribution of Intralipid-20% [35]. The mean diameter is 214.3 nm. (b,c) Total correlation function  $H_{\alpha\beta}(\theta)$  at the volume fraction of  $\eta = 20\%$  for (b) different diameter pairs and (c) wavelengths.

For the numerical computations of the FST and ZST, we used in-house codes written in MATLAB based on the textbook [4,21] and open sources for the Mie theory [36,37]. The discrete step size of the angles  $\theta$  and  $\phi$  is 0.005 [rad]. The computational time of the ZST at each volume

fraction and wavelength was approximately 6 seconds with a single CPU, while the time of the FST was 12 hours. For other details of the numerical computations of the FST and ZST, see Refs. [29], where the FST and ZST are called dependent and independent scattering theories, respectively.

Figures 2(b) and (c) show the total correlation functions  $H_{\alpha\beta}(\theta)$  using the polydisperse PY model at different diameter pairs and wavelengths with  $\eta = 20\%$ , respectively. The complicated dependence of  $H_{\alpha\beta}(\theta)$  on the pair of the diameter classes,  $\lambda$ , and  $\eta$  contributes to the results of the scattering properties. We preliminarily confirmed that the function's contribution for the pair of the same and large diameters is dominant over those for the other pairs.

## 2.2. Radiative transfer theory (RTT) for a random medium

As the macroscopic-scale colloidal suspension, we consider the semi-infinite homogeneous medium in the three dimensions (3D). Time and length scales of light propagation based on the RTT are categorized into ballistic and diffusive regimes. Experimental works [1,38] and our numerical works [39] have evaluated the crossover length from the ballistic to diffusive regimes as approximately  $10/(\mu'_s + \mu_a)$ , where  $\mu_a$  is the absorption coefficient. In this study, the scattering properties vary with the volume fraction and wavelength, and hence the crossover length also varies. As shown in Fig. 1(b), the inverse of  $\mu_s$  corresponds to the mean free path length between the radiation (light intensity) and medium in the ballistic regime, while the inverse of  $\mu'_s$  to the length in the diffusive regime. The radiative transfer equation (RTE) is valid in the two regimes, while the photon diffusion equation (PDE) is only valid in the diffusive regime.

### 2.2.1. Analytical solutions of the RTE for a 3D semi-infinite homogeneous medium

We employed an analytical solution of the RTE for the semi-infinite medium under the diffuse refractive-index mismatched boundary condition at  $z = 0$ , expressed in the form of the fluence rate  $\Phi_{RTE}(\mathbf{r}, t)$ .  $\Phi_{RTE}(\mathbf{r}, t)$  is based on the analytical solution  $\Phi_{LK}$  of the RTE for an infinite medium derived by Liemert and Kienle [40]. The verification of  $\Phi_{RTE}$  and  $\Phi_{LK}$  has been confirmed by several independent works [41,42] using the Monte-Carlo simulations and ours [43,44] using the numerical calculations of the RTE with different schemes. See the Ref. [45] for the details of the RTT (RTE and PDE) and numerical calculations of the analytical solution for the semi-infinite medium.

### 2.2.2. Numerical conditions of the RTT combined with the EMT

In this study, we employed a multi-scale light propagation model based on the RTE combined with the FST or ZST (RTE-FST or RTE-ZST). As listed in Table 1, we used the scattering properties calculated from the FST or ZST in the calculations of the RTE. The  $\mu_a$ -value is simply fixed at  $0.1 \text{ cm}^{-1}$  to focus the light scattering process, modeling a situation that we slightly added an absorber such as India ink to the colloidal suspension. For details of the light propagation models, please refer to [29]. The refractive index of the colloidal suspension is given as  $n_{cs}(\eta, \lambda) = \eta' n_s(\lambda) + (1 - \eta') n_w(\lambda)$  with  $\eta' = \eta/100$  [2]. The speed of light  $v$  for the colloidal suspension is given as  $c/n_{cs}$  with the speed of light  $c$  in vacuum, meaning that  $v$  depends on  $\eta$  and  $\lambda$ . The source was set inside the medium by a small positive value of  $1/\mu'_s$  in the  $z$ -direction from the origin. The detector was set at the boundary ( $z = 0$ ) in the  $\rho$ -direction of 1.0, 1.5, and 2.0 cm as shown in Fig. 1(b). Because the source position is near the origin, the source-detector (SD) distance  $r_{sd}$  is almost equivalent to  $\rho$ . We evaluated the peak time of the fluence rate  $\Phi_{RTE}$ , which is one of the characteristic times of light propagation. We examine the dependence of the peak time on  $\eta$ ,  $\lambda$ , and  $r_{sd}$ .

**Table 1. Optical properties for two kinds of multi-scale light propagation models.  $\hat{P}_F(\eta, \lambda)$  and  $\hat{P}_Z(\lambda)$  represent the normalized phase function for the FST and ZST, respectively.**

Model	$\mu_s$ [cm <sup>-1</sup> ]	$g$ [-]	$\hat{P}$ [sr <sup>-1</sup> ]	$n$ [-]
RTE-FST	$\mu_{s,F}(\eta, \lambda)$	$g_F(\eta, \lambda)$	$\hat{P}_F(\eta, \lambda)$	$n_{cs}(\eta, \lambda)$
RTE-ZST	$\mu_{s,Z}(\eta, \lambda)$	$g_Z(\lambda)$	$\hat{P}_Z(\lambda)$	$n_{cs}(\eta, \lambda)$

### 2.3. Model equations

To examine numerical results using the FST and RTE-FST in the ranges of  $\eta$  and  $\lambda$ , we developed model equations for the scattering properties and the peak time of the fluence rate.

#### 2.3.1. Scattering properties

We start with the approximation of the phase function for the FST,  $P_F(\theta, \phi; \eta, \lambda)$  (Eq. (1)). In addition to  $H_{\alpha\beta}(\theta; \eta, \lambda)$ , we consider the static structure factor  $S_{\alpha\beta}(\theta; \eta, \lambda) = \delta_{\alpha\beta} + H_{\alpha\beta}(\theta; \eta, \lambda)$ , where  $\delta_{\alpha\beta}$  denotes Kronecker delta.  $H_{\alpha\beta}(\theta; \eta, \lambda)$  can be expanded in terms of  $\eta$  [46] as  $\sum_{i=1}^{\infty} E_{\alpha\beta,i}(\theta; \lambda)\eta^i$  with the  $i$ th-order expansion coefficient  $E_{\alpha\beta,i}(\theta; \lambda)$ .

Instead of theoretical calculation of the expansion coefficients  $E_{\alpha\beta,i}$  up to infinite order, we propose a model equation for the phase function  $P_M$  by approximating the  $\eta$ -expansion of  $S_{\alpha\beta}$  to the exponential form:

$$P_M(\theta, \phi; \eta, \lambda) = C_{01}(\theta, \phi; \lambda)\eta \exp[-C_{02}(\theta, \phi; \lambda)\eta], \quad (5)$$

where the coefficient  $C_{01}(\theta, \phi; \lambda) = \sum_{\alpha=1}^{N_s} f_{\alpha} |F_{\alpha}^{Mie}|^2 / v_0$  represents contributions of the zeroth-order expansion of  $P_F$  with  $S_{\alpha\beta} = \delta_{\alpha\beta}$ . By the assumption of the exponential form, we only have to determine the single effective coefficient  $C_{02}(\theta, \phi; \lambda)$  instead of calculating the expansion coefficients  $E_{\alpha\beta,i}$  ( $i = 1, 2, \dots, \infty$ ). By integrating  $P_M$  (Eq. (5)) over the whole solid angle, the model equation for the scattering coefficient  $\mu_{s,M}(\eta, \lambda)$  is obtained as

$$\mu_{s,M}(\eta, \lambda) = C_{s1}(\lambda)\eta \exp[-C_{s2}(\lambda)\eta], \quad C_{s1}(\lambda) = \mu_{s,Z}/v'_0, \quad (6)$$

with  $v'_0 = \sum_{\alpha} \pi d_{\alpha}^3 n_{\alpha} / 6$ . The coefficients  $C_{s1}(\lambda)$  and  $C_{s2}(\lambda)$  represent the contributions of the single-particle scattering and interference, respectively, and they are independent of  $\eta$ . The model equation  $\mu_{s,M}$  allows us to examine the contributions of the single-particle scattering and interference separately, while in the formulation of  $\mu_{s,F}$  (Eq. (2)) for the FST, the two contributions are coupled. In this study, we determined a value of  $C_{s2}(\lambda)$  by inverse analysis to minimize a difference in results of  $\mu_{s,M}$  (Eq. (6)) and  $\mu_{s,F}$  (Eq. (2)). We adopted the exponential form of the scattering coefficient with  $\eta$  in Eq. (6) based on the theory of the transport properties of colloidal particles (e.g., viscosity). It is known that the exponential form can describe the transport properties at different volume fractions [47,48]. The scattering coefficient is one of the transport properties of photons.

Using Eqs. (5) and (6), we obtain the model equations for the anisotropy factor  $g_M(\eta, \lambda)$  and the reduced scattering coefficient  $\mu'_{s,M}(\eta, \lambda)$  as

$$g_M(\eta, \lambda) = C_{g1}(\lambda) \exp[-C'_{g2}(\lambda)\eta] \sim C_{g1}(\lambda) - C_{g2}(\lambda)\eta, \quad C_{g1}(\lambda) = g_Z, \quad (7)$$

$$\mu'_{s,M}(\eta, \lambda) = (1 - g_M)\mu_{s,M} \sim C_{p1}(\lambda)\eta \exp[-C_{p2}(\lambda)\eta], \quad C_{p1}(\lambda) = \mu'_{s,Z}/v'_0. \quad (8)$$

In Eq. (7), the exponential form of anisotropy factor with  $\eta$  can be linear based on the fact that previous research works, including ours, have shown the linear dependence of  $g$  for colloidal suspensions [23,29]. This fact suggests the small value of the coefficient  $C'_{g2}$ . Although both

the formulations can describe the FST results, we choose the linear form for simplicity. We can obtain the model equation for  $\mu'_s$  using the equations for  $\mu_s$  and  $g$  in Eq. (8). This case, however, requires the pre-calculations of  $\mu_s$  and  $g$ , and the number of the coefficients for the model equation is four. In experimental studies of dense media, we frequently encounter a situation where we can evaluate the  $\mu'_s$ -value while we can't evaluate the values of  $\mu_s$  and  $g$  easily. For this case, the rightmost expression in Eq. (8) is helpful because the number of the coefficients is two, and the form does not require the pre-calculations of  $\mu_s$  and  $g$ . The coefficients  $C_{g1}(\lambda)$  and  $C_{p1}(\lambda)$  represent the contributions of the single-particle scattering, and they can be determined theoretically. The coefficients  $C_{g2}(\lambda)$  and  $C_{p2}(\lambda)$  represent the contributions of the interference, and they are determined by inverse analysis.

### 2.3.2. Peak time of the fluence rate

To develop a model equation for  $t_p$ , we need to clarify the dependence of  $t_p$  on the SD distance  $r_{sd}$  and optical properties. In our preliminary study, the temporal profiles calculated from the RTE-FST nicely agree with those from the PDE combined with the FST at  $\eta \geq 1\%$  in the whole ranges of  $\lambda$  and  $r_{sd}$  studied here. This fact indicates that the diffusion approximation holds. In the next section, we discuss the dependence of  $t_p$  by the PDE and develop a model equation for  $t_p$  by the numerical results and model equation for  $\mu'_s$ .

## 3. Numerical results

### 3.1. Scattering properties by the first-order and zeroth-order scattering theories (FST and ZST)

We examined the interference effect on the scattering properties ( $\mu_s$ ,  $g$ ,  $\mu'_s$ ) by the FST and ZST for Intralipid solutions at different volume fractions  $\eta$  up to 20% in the wavelength range  $\lambda$  from 600 to 980 nm.

Figure 3 compares the scattering properties for the FST (Eqs. (2), (3), (4)) with those for the ZST at  $\lambda = 680, 759, 860$  nm. At a low volume fraction, the results for the FST almost agree with those for the ZST. At a higher volume fraction, meanwhile, the results for the FST are smaller than those for the ZST. This result indicates the enhancement of the interference effect. The relative differences in the scattering properties between the FST and ZST are shown at each bottom panel of Fig. 3. We defined the relative difference as  $100 \times [R(ZST) - R(FST)]/R(FST)$ , where  $R(ZST)$  and  $R(FST)$  represent the results for the ZST and FST, respectively. The relative difference in  $\mu_s$  is larger than 10% at  $\eta > 3\%$  and reaches approximately 90% at  $\eta = 20\%$ , while those in  $g$  and  $\mu'_s$  are larger than 10% at  $\eta > 8\%$  and reach approximately 30% at  $\eta = 20\%$ . The small values for the FST are caused by the negative values of the term for the interference (e.g., the second term in the right-hand side of Eq. (2) for  $\mu_{s,F}$ ). The negative values of the interference term mean that the destructive interference is dominant over the constructive interference.

At a longer wavelength, the scattering properties are smaller at a fixed  $\eta$ . The reduced scattering coefficient is modeled as a power law which generally decreases with the wavelength [9,15]. The relative differences between the FST and ZST depend less on the wavelength. This result suggests the less  $\lambda$ -dependence of the volume fraction range where the interference effects are enhanced. The scattering properties values for Intralipid-20% (current work) are larger than those for Intralipid-10% (our previous work [29]) at the same volume fraction and wavelength. This result is because of the difference in the size distribution. The mean diameter for Intralipid-20% is approximately twice as large as that for Intralipid-10%.

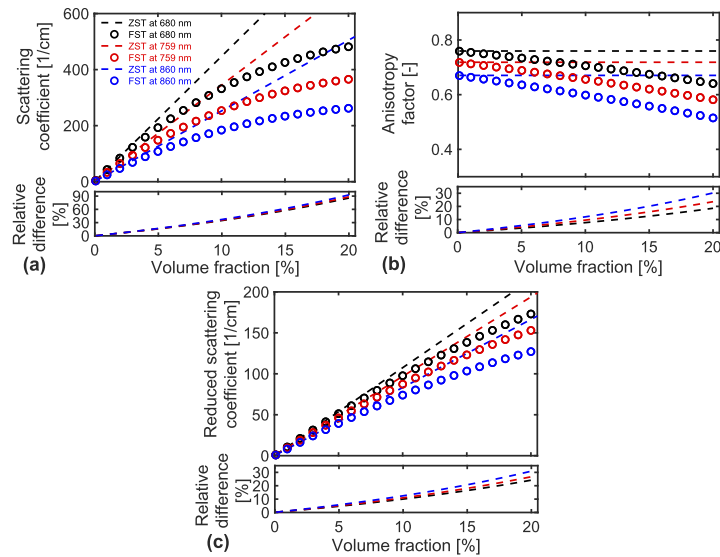


**Fig. 3.** Scattering properties for the FST (Eqs. (2), (3), (4)) and ZST at different volume fractions  $\eta$  up to 20% and wavelengths  $\lambda = 680, 759, 860$  nm in Intralipid solutions. (a) Scattering coefficient  $\mu_s$ , (b) anisotropy factor  $g$ , and (c) reduced scattering coefficient  $\mu'_s$ . Relative differences in the scattering properties between the FST and ZST are plotted at each figure's bottom.

### 3.2. Comparison of numerical results for the scattering properties with measurement data

To validate our numerical calculations, we compared the numerical results of  $\mu_s$  and  $\mu'_s$  for the FST with measurement data in Intralipid solutions by Wen *et al.* [15] and data by Zaccanti *et al.* [27].

As shown in Fig. 4(a), the numerical results of  $\mu'_s$  for the FST nicely agree with measurement data by Wen *et al.* at a longer wavelength than 700 nm. Below 700 nm, the numerical results are different from measurement data by Wen *et al.*. Meanwhile, the numerical result agrees with a measurement result by Zaccanti *et al.* at 633 nm. The difference probably comes from the difference in the particle size distribution. At the lower wavelength, the  $\mu'_s$ -value is larger. Hence, the difference in the  $\mu'_s$ -value likely is enhanced at the lower wavelength. Figures 4(b) and (c) compare the numerical results for the FST with measurement data by Zaccanti *et al.* [27] at different volume fractions and the wavelength of 633 nm. We can see agreements between the numerical and experimental results primarily for the reduced scattering coefficient. These agreements validate our numerical calculations of the FST with the PY model. The agreements also indicate that the interference, considered for the FST, mainly contributes to the scattering properties at the present volume fraction range. These results are consistent with previous research works such as monodisperse silica suspension [23].

### 3.3. Temporal profiles of the fluence rate by the RTE-FST and RTE-ZST

We investigated temporal profiles of the fluence rates  $\Phi$  using the multi-scale light propagation models, RTE-FST and RTE-ZST, as listed in Table 1 to examine the interference effects on light propagation. Figure 5(a) shows that the  $\Phi$ -results agree with each other at  $\eta = 1\%$ , while the  $\Phi$ -results for the ZST largely differ from those for the FST at  $\eta = 20\%$ . These results are similar to the results of the scattering properties in Fig. 3. The differences in  $\Phi$  mainly come from

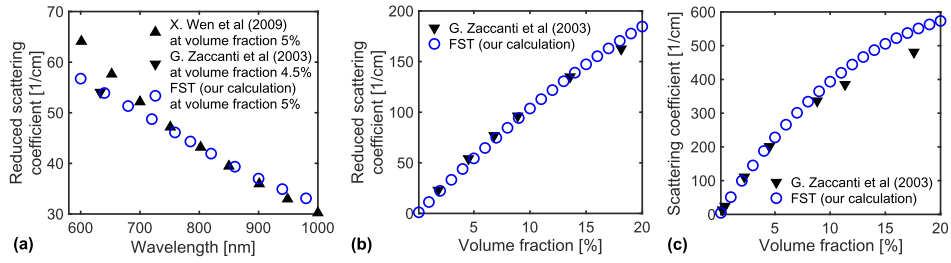


**Fig. 4.** (a) Reduced scattering coefficients at different wavelengths: measurement data by X. Wen *et al.* [15] with  $\eta = 5\%$  and by G. Zaccanti *et al.* [27] with  $\eta = 4.5\%$ , and numerical results for the FST with  $\eta = 5\%$ . (b,c) Reduced scattering and scattering coefficients at different volume fractions: measurement data by G. Zaccanti *et al.* [27] at  $\lambda = 633$  nm and numerical results for the FST at  $\lambda = 633$  nm.

those in  $\mu'_s$  between the FST and ZST because our preliminary study showed that the diffusion approximation holds at  $\eta \geq 1$

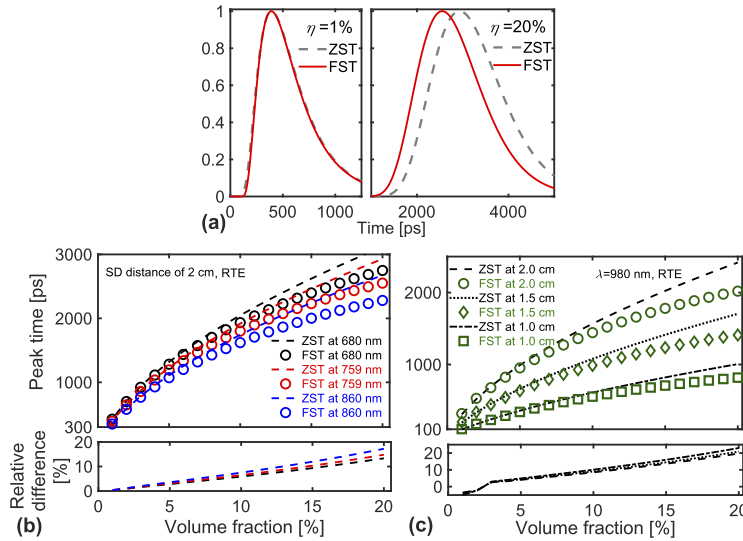


**Fig. 5.** (a) Temporal profiles of the fluence rate  $\Phi$  normalized by their peak values for the RTE-FST and RTE-ZST at different volume fractions  $\eta$  at  $\lambda = 759$  nm and SD distance  $r_{sd} = 2.0$  cm. (b,c) Peak times  $t_p$  of the fluence rate using the RTE-FST and RTE-ZST (on the top), and the relative differences in  $t_p$  (at the bottom). The results are at (b) different values of  $\lambda$  with  $r_{sd} = 2.0$  cm and at (c) different values of  $r_{sd}$  with  $\lambda = 980$  nm.

We evaluated the peak times  $t_p$  of  $\Phi$  at different values of  $\eta$ ,  $\lambda$ , and  $r_{sd}$  as shown in Figs. 5 (b) and (c). The differences in  $t_p$  between the RTE-FST and RTE-ZST become larger as  $\eta$  increases, meaning the strong influence of the interference on light propagation. For the RTE-ZST,  $t_p$  is not linearly proportional to  $\eta$ , different from the  $\eta$ -dependence of the scattering properties for the ZST (linear dependence in Fig. 3). At a longer SD distance, the  $t_p$ -value becomes larger, meaning the photon path length from the source to the detector becomes longer.

### 3.4. Model equations

#### 3.4.1. Scattering properties

We examined the complicated behaviors of the scattering properties for the FST by the model equations developed here. Figures 6(a)-(c) show that the model equations (Eqs. (6), (7), (8)) nicely agree with the scattering properties for the FST by adjusting the values of  $C_{m2}$  ( $m = \{s, g, p\}$ ). The R-squared values for the model equations range from 0.995 to 0.999. At each figure's bottom, we plot the relative differences in the scattering properties between the model equations and FST, defined as  $100 \times [R(Model) - R(FST)]/R(FST)$  with the results for the model equations  $R(Model)$ . The absolute values of the differences are less than 1.5%. Figures 6(d) and (e) show the wavelength-dependence of the coefficients  $C_{m1}$  and  $C_{m2}$ , where  $C_{s1}$  and  $C_{p1}$  are normalized by  $\lambda^{-1}$  to be dimensionless.  $\lambda C_{s1}$  and  $\lambda C_{p1}$  are almost constant as a function of  $\lambda$ ; the linear slope values are evaluated as  $-0.47 \times 10^{-3}$  and  $-0.78 \times 10^{-5}$  in the unit of  $\lambda[\text{nm}]$ , respectively. The results suggest that  $C_{s1}$  and  $C_{p1}$  are mainly proportional to  $\lambda^{-1}$ ;  $C_{s1}[\text{1/cm}] \sim 0.63 \times 10^8 \lambda^{-1}$  and  $C_{p1}[\text{1/cm}] \sim 0.08 \times 10^8 \lambda^{-1}$ , respectively. Meanwhile, the other coefficients of  $C_{g1}$ ,  $C_{s2}$ ,  $C_{g2}$ , and  $C_{p2}$  change linearly with the  $\lambda$ -change, but the linear slope values are small ( $\sim 10^{-3}$ ). The stronger  $\lambda$ -dependences of  $C_{s1}$  and  $C_{p1}$  than those of  $C_{s2}$  and  $C_{p2}$  indicate that the single-particle scattering is dominant for  $\mu_s$  and  $\mu'_s$  over the interference. The slope values for  $C_{s2}$ ,  $C_{g2}$ , and  $C_{p2}$  are almost the same, suggesting the similar contributions of the interference effect on the scattering properties. In Eqs. (6), (7), (8),  $C_{m1}$  relates with the scattering properties for the ZST. The increase in wavelength with a fixed diameter corresponds to the decrease in diameter with a fixed wavelength in terms of the size parameter  $x_s$ . Generally, the values of  $\mu_s$  and  $\mu'_s$  reduce, and the  $g$ -value approaches zero with the smaller diameter or longer wavelength because of the smaller amount of induced dipole moments in the particle [2]. The  $\lambda$ -dependence of  $C_{m1}$  is consistent with the general behavior of the scattering properties. The increase in  $C_{m2}$  with increasing  $\lambda$  means the enhancement of the interference. The zero values of  $C_{m2}$  mean no interference effect. The linear  $\lambda$ -dependence of  $C_{m2}$  suggests that  $C_{m2}$  is probably specified by  $\lambda/r_{im}$  with the mean intermolecular distance  $r_{im}$ .

The computational time of the FST was approximately 12 hours at each volume fraction and wavelength. Meanwhile, the time of the model equations was within a second, including the inverse analysis process of the coefficients, thanks to their analytical forms. We note that the parallel computing of the FST is not easy because the computation requires the summation with the five variables or indices:  $\theta, \phi, \alpha, \beta, \gamma$ , where  $\gamma$  is the index for the amplitude function of Mie theory. These facts mean the high computational efficiency of the model equations.

#### 3.4.2. Peak time of the fluence rate

For developing a model equation for  $t_p$ , we examined the dependence of  $t_p$  on  $r_{sd}$  and the optical properties by the PDE. In an infinite medium, the analytical form of the peak time  $t_{p,inf}$  for the PDE is given as

$$t_{p,inf} = \left[ -3 + 2\sqrt{3r_{sd}^2\mu_a\mu'_s + 9/4} \right] (4\mu_a\nu)^{-1}. \quad (9)$$

The analytical form suggests that when  $t_{p,inf}$  and  $r_{sd}$  are normalized by  $\mu_a\nu$  and  $\sqrt{\mu_a\mu'_s}$ , respectively, the  $t_{p,inf}$ -results at different values of  $r_{sd}$  and optical properties are collapsed on a single curve. We employed the normalization to the numerical results of  $t_p$  for the RTE-FST in the semi-infinite medium at different values of  $r_{sd}$ ,  $\mu'_s$ , and  $n_{cs}$ , where  $\mu'_s$  and  $n_{cs}$  vary with  $\eta$  and  $\lambda$ . Figure 7(a) shows that the normalized peak times  $\hat{t}_p = t_p\mu_a\nu$  for the RTE-FST are collapsed on a single curve for the normalized SD distances  $\hat{r}_{sd} = r_{sd}\sqrt{\mu_a\mu'_s}$ , indicating the validity of the normalization. The single curve of  $\hat{t}_p$  is fitted by a power function  $D_1\hat{r}_{sd}^{D_2}$  with dimensionless fitting coefficients  $D_1 \sim 0.4$  and  $D_2 \sim 1.3$  and the R-squared value of 0.999.

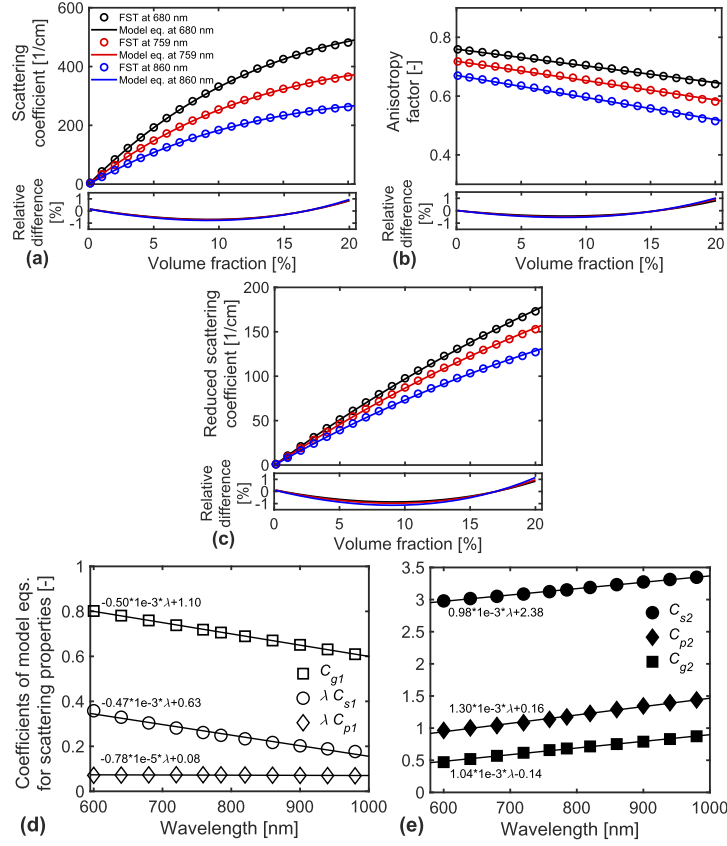


**Fig. 6.** (a-c) Comparisons of the model equations (Eqs. (6), (7), (8)) with the scattering properties for the FST. The other details are the same as Fig. 3. (d,e) Coefficients of the model equations for the scattering properties in the  $\lambda$ -range from 600 to 980 nm.

Using the power function of  $\hat{t}_p$  and the form of  $\mu'_{s,M}$  (Eq. (8)), we obtain the model equation for the peak time of the fluence rate  $t_{p,M}$  as

$$t_{p,M}(\eta, \lambda) = C_{t1}(\lambda) [\eta \exp(-C_{p2}(\lambda)\eta)]^{D_2/2}, \quad (10)$$

$$C_{t1}(\lambda) = D_1[\mu_a v(\lambda)]^{-1} r_{sd}^{D_2} [\mu_a C_{p1}(\lambda)]^{D_2/2}.$$

Although the coefficient  $C_{t1}$  depends on  $\eta$  via  $v = c/n_{cs}$ , the  $\eta$ -dependence of  $C_{t1}$  is very weak compared with the  $\lambda$ -dependence. Equation (10) includes the coefficient  $C_{p2}$ , which is originally defined in the model equation for  $\mu'_s$  (Eq. (8)). The relation between  $t_{p,M}$  and  $C_{p2}$  corresponds to a relationship between the characteristic time of light propagation on the macroscopic scale and interference on the microscopic scale.

Figures 7(b) and (c) show the model equations  $t_{p,M}$  (Eq. (10)) agree well with the numerical results of  $t_p$  for the RTE-FST with the range of the R-squared values from 0.988 to 0.999. As shown in each figure's bottom, the relative differences between the model equations and RTE-FST are larger at a lower volume fraction. The smallest R-squared value of 0.988 is obtained in the case of  $\lambda = 980$  nm and  $r_{sd} = 1.0$  cm as shown in Fig. 7(c). This is probably because as shown in Fig. 7(a), the power function for  $\hat{t}_p$  slightly deviates from the results using the FST at the short distance region ( $\hat{r}_{sd} \lesssim 2$ ). We examined mean values of the coefficient  $C_{t1}$  over  $\eta$  as shown in Fig. 7(d). The mean value decreases linearly with  $\lambda$ , different from the behaviors of

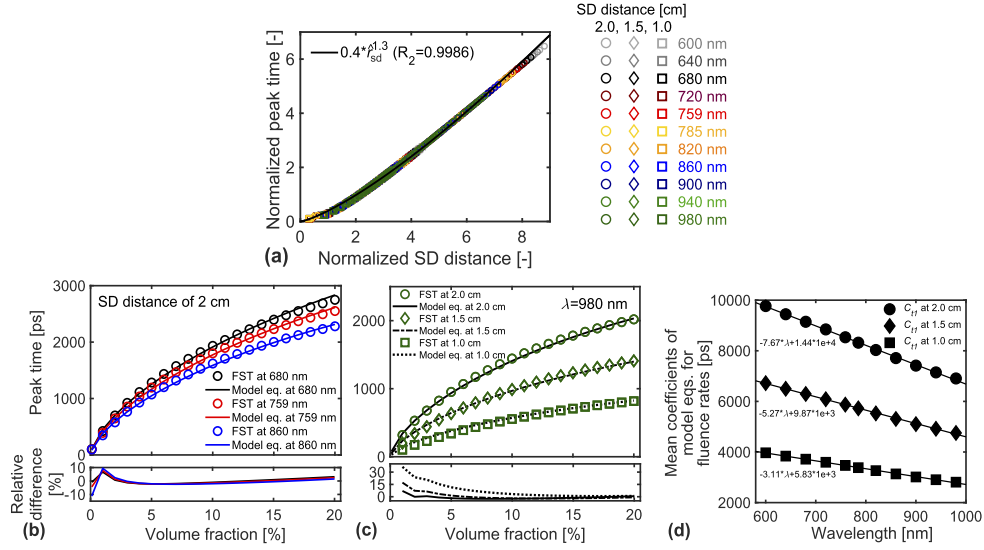


**Fig. 7.** (a) Normalized peak times  $\hat{t}_p = t_p \mu_a v$  for the RTE-FST as a function of normalized SD distance  $\hat{r}_{sd} = r_{sd} \sqrt{\mu_a \mu'_s}$  at different values of  $\lambda$  and  $\eta$  with a power function (solid curve). (b,c) Comparisons of the peak times for the model equation (Eq. (10)) with the numerical results for the RTE-FST. The other details are the same as Figs. 5(b) and (c). (d) Mean values of the coefficients  $C_{i1}$  over  $\eta$  as a function of  $\lambda$  with linear functions (solid lines).

$C_{p1} \sim 1/\lambda$ . The slope value of  $C_{i1}$  with  $\lambda$  depends on  $r_{sd}$ , resulting in the complicated behavior of  $t_p$ . Similarly to the results of  $\mu_s$  and  $\mu'_s$ , the  $\lambda$ -dependence of  $t_p$  is mainly caused by the single-particle scattering compared with the interference, because the  $\lambda$ -dependence of  $C_{i1}$  is stronger than those of  $C_{p2}$  as shown in Figs. 7(d) and 6(e).

### 3.4.3. Dimensionless analysis

Using the model equations (Eqs. (6)-(10)), we performed the dimensionless analysis of the scattering properties and peak time of the fluence rate. We consider the normalization of the model equations as

$$\hat{\mu}_{s,M} = \hat{\eta} \exp(-\hat{\eta}), \quad \hat{\mu}_{s,M} = \mu_{s,M} C_{s2} / C_{s1}, \quad \hat{\eta} = C_{s2} \eta, \quad (11)$$

$$\hat{g}_M = -\hat{\eta}, \quad \hat{g}_M = g_M - C_{g1}, \quad \hat{\eta} = C_{g2} \eta, \quad (12)$$

$$\hat{\mu}'_{s,M} = \hat{\eta} \exp(-\hat{\eta}), \quad \hat{\mu}'_{s,M} = \mu'_{s,M} C_{p2} / C_{p1}, \quad \hat{\eta} = C_{p2} \eta, \quad (13)$$

$$\hat{t}_{p,M} = [\hat{\eta} \exp(-\hat{\eta})]^{D_2/2}, \quad \hat{t}_{p,M} = t_{p,M} C_{p2}^{D_2/2} / C_{i1}, \quad \hat{\eta} = C_{p2} \eta. \quad (14)$$

The normalized model equations suggest that when the numerical results for the FST and RTE-FST at different values of  $\lambda$  and  $r_{sd}$  by the coefficients for the model equations, the numerical results would be collapsed on single curves regardless of  $\lambda$  and  $r_{sd}$ . We can observe the collapsing of the numerical results on the single curves in Fig. 8. As shown in Fig. 8(a), the normalized results of  $\mu_{s,F}$  and  $\mu'_{s,F}$  are collapsed on the same single curve. This result indicates the same contribution of the interference for  $\mu_s$  and  $\mu'_s$ .

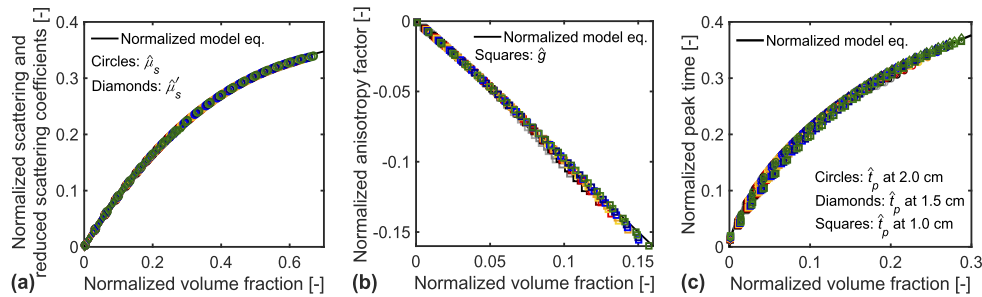


**Fig. 8.** Normalized scattering properties for the FST and peak times for the RTE-FST as a function of normalized volume fraction based on the coefficients of the model equations (Eqs. (11)-(14)) at different wavelengths. Each color of the markers corresponds to the results at each wavelength in the same way of Fig. 7(a).

#### 4. Conclusions

We have developed the model equations for  $\mu_s$ ,  $g$ ,  $\mu'_s$ , and  $t_p$  to examine the interference effects for the polydisperse colloidal suspensions at different volume fractions in the near-infrared wavelength range. We have shown that the model equations can describe well the numerical results calculated from the FST and RTE-FST with the two coefficients, denoted by  $C_{l1}$  ( $l = \{s, g, p, t\}$ ) and  $C_{m2}$  ( $m = \{s, g, p\}$ ). Using the model equations, we have evaluated the factors of the interference represented by  $C_{m2}$ , separately from those of the single-particle scattering by  $C_{l1}$ . We have found the linear relation of the interference factors with the wavelength. Dimensionless analysis by the model equations has shown the simple mechanism of the interference effects, regardless of the wavelength and source-detector distance. This result suggests there is the universal behavior of the interference effects. It is straightforward to develop the model equations for monodisperse systems such as silica suspensions from the equations for polydisperse systems developed here. The model equations have the potential for examining measurement data of the scattering properties for various kinds of colloidal suspensions (e.g., charged suspensions) at various wavelength ranges. In the current study, we have prior information on the particle size distribution and refractive index for the colloidal suspension. Using the information, we calculated theoretically the coefficients  $C_{l1}$  without fitting. However, even if we don't have the prior information, the model equation allows examining the experimental and numerical results by inverse analysis of the coefficients  $C_{l1}$  and  $C_{m2}$ . The examination is challenging as future work.

**Funding.** Japan Society for the Promotion of Science (20H02076, 21H05577).

**Acknowledgments.** We would like to thank Dr. L. Tsang and G. Nishimura for fruitful comments from theoretical and experimental point of view, respectively.

**Disclosures.** The authors declare no conflicts of interest.

**Data availability.** Data underlying the results presented in this paper are not publicly available at this time but may be obtained from the authors upon reasonable request.

#### References

1. V. Ntziachristos, "Going deeper than microscopy: The optical imaging frontier in biology," *Nat. Methods* **7**(8), 603–614 (2010).
2. V. V. Tuchin, *Tissue optics : light scattering methods and instruments for medical diagnosis* (SPIE Press, 2015).
3. L. V. Wang and H. Wu, *Biomedical Optics: Principles and Imaging* (John Wiley & Sons, Ltd, 2009).
4. L. Tsang, J. A. Kong, and K.-H. Ding, *Scattering of Electromagnetic Waves: Theories and Applications* (John Wiley & Sons, Ltd, 2000).

5. J. Moreira, B. Serrano, A. Ortiz, and H. D. Lasa, "Evaluation of Photon Absorption in an Aqueous TiO<sub>2</sub> Slurry Reactor Using Monte Carlo Simulations and Macroscopic Balance," *Ind. Eng. Chem. Res.* **49**(21), 10524–10534 (2010).
6. Y. Hoshi and Y. Yamada, "Overview of diffuse optical tomography and its clinical applications," *J. Biomed. Opt.* **21**(9), 091312 (2016).
7. Y. Yamada, H. Suzuki, and Y. Yamashita, "Time-Domain Near-Infrared Spectroscopy and Imaging : A Review," *Appl. Sci.* **9**(6), 1127–1154 (2019).
8. S. Okawa, Y. Hoshi, and Y. Yamada, "Improvement of image quality of time domain diffuse optical tomography with lp sparsity regularization," *Biomed. Opt. Express* **2**(12), 3334–3348 (2011).
9. J. Qin and R. Lu, "Measurement of the optical properties of fruits and vegetables using spatially resolved hyperspectral diffuse reflectance imaging technique," *Postharvest Biol. Technol.* **49**(3), 355–365 (2008).
10. Y. Hoshi, Y. Tanikawa, E. Okada, H. Kawaguchi, M. Nemoto, K. Shimizu, T. Kodama, and M. Watanabe, "In situ estimation of optical properties of rat and monkey brains using femtosecond time-resolved measurements," *Sci. Rep.* **9**(1), 9165 (2019).
11. A. N. Bashkatov, E. A. Genina, and V. V. Tuchin, "OPTICAL PROPERTIES OF SKIN, SUBCUTANEOUS, AND MUSCLE TISSUES : A REVIEW," *J. Innov. Opt. Health Sci.* **04**(1), 9–38 (2011).
12. M. Friebel, A. Roggan, G. Müller, and M. Meinke, "Determination of optical properties of human blood in the spectral range 250 to 1100 nm using Monte Carlo simulations with hematocrit-dependent effective scattering phase functions," *J. Biomed. Opt.* **11**(3), 034021 (2006).
13. S. Chandrasekhar, *Radiative Transfer* (Dover, 1960).
14. F. Long, F. Li, X. Intes, and S. P. Kotha, "Radiative transfer equation modeling by streamline diffusion modified continuous Galerkin method," *J. Biomed. Opt.* **21**(3), 036003 (2016).
15. X. Wen, V. V. Tuchin, Q. Luo, and D. Zhu, "Controlling the scattering of Intralipid by using optical clearing agents," *Phys. Med. Biol.* **54**(22), 6917–6930 (2009).
16. F. Foschum and A. Kienle, "Optimized goniometer for determination of the scattering phase function of suspended particles: simulations and measurements," *J. Biomed. Opt.* **18**(8), 085002 (2013).
17. W. Chang, K. H. Ding, L. Tsang, and X. Xu, "Microwave Scattering and Medium Characterization for Terrestrial Snow with QCA-Mie and Bicontinuous Models: Comparison Studies," *IEEE Trans. on Geoscience and Remote Sensing* **54**(6), 3637–3648 (2016).
18. L. L. Foldy, "The Multiple Scattering of Waves. I. General Theory of Isotropic Scattering by Randomly Distributed Scatterers," *Phys. Rev.* **67**(3-4), 107–119 (1945).
19. M. Lax, "Multiple Scattering of Waves. II. The Effective Field in Dense Systems," *Phys. Rev.* **85**(4), 621–629 (1952).
20. M. I. Mishchenko, "Independent and dependent scattering by particles in a multi-particle group," *OSA Continuum* **1**(1), 243–260 (2018).
21. L. Tsang, J. A. Kong, K.-H. Ding, and C. O. Ao, *Scattering of Electromagnetic Waves: Numerical Simulations* (John Wiley & Sons, Ltd, 2001).
22. H. J. V. Stavereen, C. J. M. Moes, J. V. Marie, S. A. Prah, and M. J. C. V. Gemert, "Light scattering in Intralipid-10 of 400-1100 nm," *Appl. Opt.* **30**(31), 4507–4514 (1991).
23. V. D. Nguyen, D. J. Faber, E. van der Pol, T. G. van Leeuwen, and J. Kalkman, "Dependent and multiple scattering in transmission and backscattering optical coherence tomography," *Opt. Express* **21**(24), 29145–29156 (2013).
24. J. D. Cartigny, Y. Yamada, and C. L. Tien, "Radiative transfer with dependent scattering by particles: part 1 - theoretical investigation," *J. Heat Transfer* **108**(3), 608–613 (1986).
25. Y. Yamada, J. D. Cartigny, and C. L. Tien, "Radiative transfer with dependent scattering by particles: part 2 - experimental investigation," *J. Heat Transfer* **108**(3), 614–618 (1986).
26. L. Tsang and J. A. Kong, "Scattering of Electromagnetic Waves from a Dense Medium Consisting of Correlated Mie Scatterers with Size Distributions and Applications to Dry Snow," *J. Electromag. Waves and Appl.* **6**(1-4), 265–286 (1992).
27. G. Zaccanti, S. D. Bianco, and F. Martelli, "Measurements of optical properties of high-density media," *Appl. Opt.* **42**(19), 4023–4030 (2003).
28. L. Bressel, R. Hass, and O. Reich, "Particle sizing in highly turbid dispersions by Photon Density Wave spectroscopy," *J. Quant. Spectrosc. Radiat. Transfer* **126**, 122–129 (2013).
29. H. Fujii, L. Tsang, J. Zhu, K. Nomura, K. Kobayashi, and M. Watanabe, "Photon transport model for dense polydisperse colloidal suspensions using the radiative transfer equation combined with the dependent scattering theory," *Opt. Express* **28**(15), 22962–22977 (2020).
30. L. F. Rojas-Ochoa, S. Romer, F. Scheffold, and P. Schurtenberger, "Diffusing wave spectroscopy and small-angle neutron scattering from concentrated colloidal suspensions," *Phys. Rev. E* **65**(5), 051403 (2002).
31. S. Fraden and G. Maret, "Multiple light scattering from concentrated, interacting suspensions," *Phys. Rev. Lett.* **65**(4), 512–515 (1990).
32. C. F. Bohren and D. R. Huffman, *Absorption and Scattering of Light by Small Particles* (John Wiley & Sons, 1983).
33. J. K. Percus and G. J. Yevick, "Analysis of Classical Statistical Mechanics by Means of Collective Coordinates," *Phys. Rev.* **110**(1), 1–13 (1958).
34. R. J. Baxter, "Ornstein-Zernike Relation and Percus-Yevick Approximation for Fluid Mixtures," *J. Chem. Phys.* **52**(9), 4559–4562 (1970).

35. V. M. Kodach, D. J. Faber, J. V. Marle, T. G. V. Leeuwen, and J. Kalkman, "Determination of the scattering anisotropy with optical coherence tomography," *Opt. Express* **19**(7), 6131–6140 (2011).
36. C. Mätzler, "MATLAB Functions for Mie Scattering and Absorption," IAP Res. Rep. **02-08**, 1 (2002).
37. C. Mätzler, "MATLAB Functions for Mie Scattering and Absorption Version 2," IAP Res. Rep. **02-11**, 1 (2002).
38. K. M. Yoo, F. Liu, and R. R. Alfano, "When does the diffusion approximation fail to describe photon transport in random media?" *Phys. Rev. Lett.* **64**(22), 2647–2650 (1990).
39. H. Fujii, S. Okawa, Y. Yamada, and Y. Hoshi, "Hybrid model of light propagation in random media based on the time-dependent radiative transfer and diffusion equations," *J. Quant. Spectrosc. Radiat. Transfer* **147**, 145–154 (2014).
40. A. Liemert and A. Kienle, "Infinite space Green's function of the time-dependent radiative transfer equation," *Biomed. Opt. Express* **3**(3), 543 (2012).
41. E. Simon, F. Foschum, and A. Kienle, "Hybrid Green's function of the time-dependent radiative transfer equation for anisotropically scattering semi-infinite media," *J. Biomed. Opt.* **18**(1), 015001 (2013).
42. F. Kamran, O. H. A. Abildgaard, A. A. Subash, P. E. Andersen, S. Andersson-Engels, and D. Khoptyar, "Computationally effective solution of the inverse problem in time-of-flight spectroscopy," *Opt. Express* **23**(5), 6937–6945 (2015).
43. H. Fujii, Y. Yamada, G. Chiba, Y. Hoshi, K. Kobayashi, and M. Watanabe, "Accurate and efficient computation of the 3D radiative transfer equation in highly forward-peaked scattering media using a renormalization approach," *J. Comput. Phys.* **374**, 591–604 (2018).
44. H. Fujii, G. Chiba, Y. Yamada, Y. Hoshi, K. Kobayashi, and M. Watanabe, "A comparative study of the delta-Eddington and Galerkin quadrature methods for highly forward scattering of photons in random media," *J. Comput. Phys.* **423**, 109825 (2020).
45. H. Fujii, M. Ueno, K. Kobayashi, and M. Watanabe, "Characteristic length and time scales of the highly forward scattering of photons in random media," *Appl. Sci.* **10**(1), 93 (2019).
46. J.-P. Hansen and I. McDonald, *Theory of Simple Liquids* (Elsevier, 2006).
47. T. Kalwarczyk, K. Sozanski, S. Jakiela, A. Wisniewska, E. Kalwarczyk, K. Kryszczuk, S. Hou, and R. Holyst, "Length-scale dependent transport properties of colloidal and protein solutions for prediction of crystal nucleation rates," *Nanoscale* **6**(17), 10340–10346 (2014).
48. E. B. Bagley, D. D. Christianson, and A. C. Beckwith, "A Test of the Arrhenius Viscosity-Volume Fraction Relationship for Concentrated Dispersions of Deformable Particles," *J. Rheol.* **27**(5), 503–507 (1983).